

Electronic properties of thin films of tensile strained HgTe

Jihang Zhu,¹ Chao Lei,¹ and Allan H. MacDonald¹

¹*Department of Physics, The University of Texas at Austin, Austin, Texas 78712, USA*

Tensile strained bulk HgTe is a three-dimensional topological insulator. Because of the energetic position of its surface state Dirac points relative to its small bulk gap, the electronic properties of the relatively thin MBE-grown films used to study this material experimentally are quite sensitive to details of its electrostatic band-bending physics. We have used an 8-band $\mathbf{k} \cdot \mathbf{p}$ model to evaluate the gate voltage dependence of its thin-film two-dimensional subbands and related thermodynamic and transport properties in films with thicknesses between 30 and 70nm, accounting self-consistently for gate field screening by the topologically protected surface states and bulk state response. We comment on the effective dielectric constant ϵ that is appropriate in calculations of this type, arguing for a smaller value $\epsilon_r \approx 6.5$ than is commonly used. Comparing with recent experiments, we find that our fully microscopic model of gate field screening alters the interpretation of some observations that have been used to characterize strained HgTe thin films.

I. INTRODUCTION

Three-dimensional(3D) topological insulators(TIs) possess 2D Dirac-like surface states that are protected by time-reversal symmetry^{1,2} and have interesting transport properties related to strong spin-momentum locking. Unintended and uncontrolled bulk doping often obscures the meaning of experiments that are intended to probe the surface state properties of the heavily studied pnictogen chalcogenide bulk TIs like Bi₂Se₃, Bi₂Te₃ and Sb₂Te₃, making it hard to distinguish surface states contributions to observables from bulk contributions. Tensile strained HgTe is an alternative 3D topological insulator³ that has the advantage of extremely low background doping, which should make it more possible to separate surface and bulk effects experimentally. Considerable progress has already been made studying strained HgTe films experimentally, including realizations of proximitied superconductivity⁴⁻⁸, the quantum Hall effect⁹ and the quantum anomalous Hall effect¹⁰.

However, the strain is practically induced by lattice mismatch in quantum wells. That is, only thin films of strained HgTe can be made experimentally. And the bulk gap of the strained HgTe thin films is proportional to the strength of tensile strain¹¹. Because of the small strain, the bulk gap is small as well. The bulk gap of the strained HgTe/CdTe quantum well is about 20meV, while the gaps of pnictogen chalcogenides are about 0.3eV. Because of the small gap, the surface state localization length is fairly large and the separation between bulk and surface effects in thin film HgTe samples that are available experimentally is not always clear. Efforts to access and verify the surface states of strained HgTe are still making^{12,13}, mainly on thin films up to thickness of 80nm.

With these motivations, we have examined the multi-band envelope description of strained HgTe thin films with thicknesses between 30 and 70nm, accounting carefully for electron-electron interactions. Our model provides a basis to interpret electronic properties of surface and bulk states, tuned by varying gate voltage in experiments¹²⁻¹⁴. We find that the films respond like

semiconductors to gates that induce electron gases, but like metals to gates that induce hole gases. We are able to provide simple explanations for recent experiments that characterize HgTe thin films using capacitance¹³ and thermopower measurements¹⁴. In particular, we find that it is not necessary to invoke phonon drag to explain the large difference in thermopower between electron and hole cases.

The paper is organized as follows. In section II we introduce the theoretical model that are used in our paper. 8-band $\mathbf{k} \cdot \mathbf{p}$ theory along with electron-electron interactions are used. The strain effect is considered by Bir-Pikus model. In section III, we discuss the dielectric constant of strained HgTe thin films and we find that it should be much smaller than the value, 21, which is widely used. In section IV, we capture the capacitance of strained HgTe quantum wells based on our established model and directly compare results with recent capacitance experiments. In section V, transport coefficient, thermopower and the Nernst coefficient

II. $\mathbf{k} \cdot \mathbf{p}$ THEORY FOR STRAINED HgTe

HgTe has a zinc-blende crystal structure which lacks inversion symmetry. The crystalline HgTe is a semimetal with conduction band (Γ_8 light-hole) and valence band (Γ_8 heavy-hole) degenerate at the Γ point. The band structure of HgTe/CdTe quantum well in [001] direction is calculated by self-consistently solving the Poisson-Schrödinger equation using the 8-band $\mathbf{k} \cdot \mathbf{p}$ approach¹⁵:

$$\begin{aligned} \sum_{n'} (H_{nn'} + \phi_H \delta_{nn'}) \psi_{n'} &= E \psi_n, \\ \nabla_z^2 V_H(z) &= -\frac{\rho(z)}{\epsilon_0 \epsilon_r} \end{aligned} \quad (1)$$

where n labels bands. $\phi_H = -eV_H$ is the Hartree potential contributed by electron-electron Coulomb interactions. The explicit form of $H_{nn'}$ is shown in Appendix

A. $\psi_n(z)$ is z -dependent component of the envelope function $F_n(\mathbf{r})$:

$$F_n(\mathbf{r}) = e^{i(k_x x + k_y y)} \psi_n(z) \quad (2)$$

where $f(\mu - \varepsilon_m(\mathbf{k}))$ is the Fermi-Dirac function and ρ_{bg} is the background charge distribution calculated in the flat band condition. We used the 2D analogy of the tetrahedron method¹⁶ when integrating over the 2D k -space above in Eq.(3). We ran simulations on TACC¹⁷.

A uniaxial strain opens a gap between Γ_8 light- and heavy-hole subbands and thus makes HgTe a semiconductor. The opened band gap is proportional to the strain strength. The strain effect is added through the Bir-Pikus Hamiltonian and replacing band structure parameters with hydrostatic and uniaxial deformation potentials (more details see appendix A)¹⁵. A 0.3% uniaxial strain is induced by the lattice mismatch between CdTe and HgTe. The uniaxial strain tensor is given by⁹:

$$\begin{pmatrix} \epsilon & 0 & 0 \\ 0 & \epsilon & 0 \\ 0 & 0 & \frac{-2C_{12}}{C_{11}}\epsilon \end{pmatrix} \quad (4)$$

with $\epsilon = 0.003$ and $C_{12}/C_{11} = 0.68$ which are chosen from¹⁵.

We show the band structure of a 60nm-thick HgTe quantum well in FIG.1a. It is under the 0.3% uniaxial strain and is in the flat band condition. Two degenerate surface states from top and bottom interfaces are shown with the red line in the 20meV bulk gap. The Dirac points are beneath the valence bands by around 100meV. These are consistent with former numerical results⁹.

FIG.1b shows the Fermi surfaces mapping onto the 2D k -space in the flat band condition. It clearly shows electrons and holes coexist at charge neutrality.

III. STATIC DIELECTRIC CONSTANT

The dielectric constant ϵ_r in Eq.(1) is usually taken to be 21¹⁸, which is the HgTe bulk dielectric constant examined by optical experiments. It includes the contributions as the following¹⁹:

$$\epsilon_r = \epsilon_\infty + \epsilon_{\text{inter}} + \epsilon_{\text{intra}} \approx 21 \quad (5)$$

where ϵ_∞ is the high-frequency dielectric constant due to all interband transitions except $\Gamma_8 - \Gamma_8$, ϵ_{inter} stems from $\Gamma_8 - \Gamma_8$ interband transitions and ϵ_{intra} is contributed by

where k_x and k_y are wave vectors. Note that they are still good quantum numbers, while k_z is replaced by the differential operator $-i\frac{\partial}{\partial z}$ because of the confinement in z direction. $\rho(z)$ in Eq.(1) is the charge density along z direction, which is discretized into N pieces in numerical calculation,

$$\rho(z_j) = \frac{-e}{\Delta z} \int \frac{d^2\mathbf{k}}{(2\pi)^2} \left[\sum_{m=1}^{8N} f(\mu - \varepsilon_m(\mathbf{k})) \sum_{n=1}^8 |\psi_n^{(m)}(z_j, \mathbf{k})|^2 \right] - \rho_{\text{bg}}(z_j) \quad (3)$$

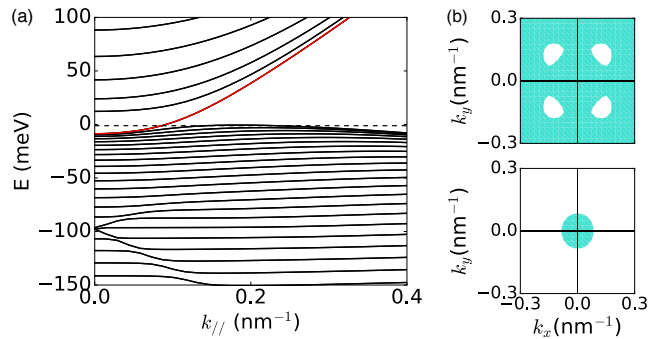


FIG. 1: (a) The band structure of 60nm HgTe quantum well with 0.3% uniaxial strain in the flat band condition. Black dashed line denotes the chemical potential. The red line shows the degenerate surface states. (b) Fermi surfaces mapping onto the 2D k -space. Aqua region is occupied while white region is unoccupied. Upper is the top valence band and lower is the surface band.

intraband transitions in Γ_8 bands. In HgTe quantum wells, however, the static dielectric constant should be dominated by transitions among bands near the Fermi level. Hence high-frequency part $\epsilon_\infty = 15.2$ ¹⁸ does not contribute to the dielectric constant of HgTe thin films. Meanwhile phonon contributions ϵ_{ph} should be considered. According to the effective charge¹⁹, phonon dielectric contribution is estimated to be $\epsilon_{\text{ph}} \approx 0.7$. As a result, HgTe quantum well dielectric constant is $\epsilon_r \approx 6.5$, much smaller than the widely used value of 21.

When the Fermi level is inside the bulk gap, where only Dirac-like surface states are occupied, a small dielectric constant helps maintain the Fermi level in the bulk gap when increasing the carrier density. It is a result of the linear dispersion and imperfect localization of the surface states. A correction term should be added into the Fermi energy-carrier density relation due to the imperfect localization of the surface states,

$$\varepsilon_F = \hbar v_F \sqrt{2\pi n_e} - \lambda \frac{e^2 l n_e}{\epsilon_0 \epsilon_r} \quad (6)$$

where l is the localization length of the surface states and λ is a constant factor capturing the effective electric

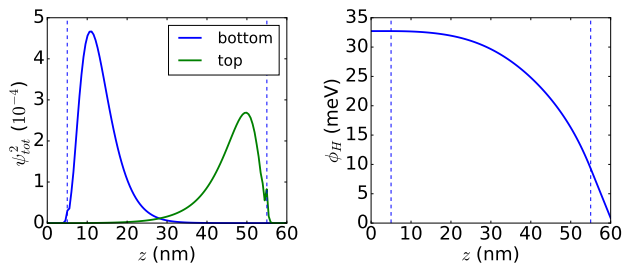


FIG. 2: Both subfigures are based on a 50nm quantum well with $\epsilon_r = 21$, carrier density is $n_e \approx 2 \times 10^{11} \text{cm}^{-2}$. The dashed lines denote the interfaces of the quantum well and barriers. (a) Probability density of bottom and top surfaces at the Fermi level. (b) Hartree potential along z .

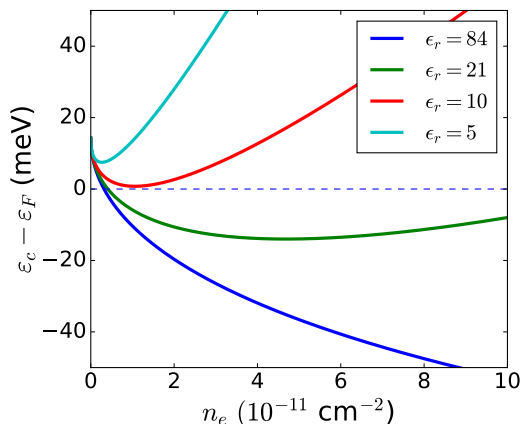


FIG. 3: Energy difference between the conduction band bottom and the Fermi level as a function of the carrier density n_e for dielectric constants $\epsilon_r = 84, 21, 10$ and 5 . In this simple model, the negative compressibility is only observable for $\epsilon_r < 10$.

field at distance l away from the top interface. Negative charges accumulate at the top interface for a positive top gate voltage. For a 50nm HgTe quantum well, l and λ can be estimated in FIG.2 to be: $l \approx 10\text{nm}$, $\lambda \approx 0.7$. By the simple model illustrated in Eq.(6), energy difference of the conduction band bottom ϵ_c and the Fermi level ϵ_F as a function of carrier density n_e for a 50nm HgTe is shown in FIG.3, where Fermi velocity is taken to be $v_F \approx 0.5 \times 10^6 \text{m/s}$ ²⁰. Negative compressibility is only observable for $\epsilon_r < 10$.

IV. QUANTUM CAPACITANCE

In HgTe quantum well experiments, a top gate voltage is usually applied to tune the Fermi level, thereby adjusting the carrier density in the system. In our theoretical model, we use the chemical potential μ as a parameter to

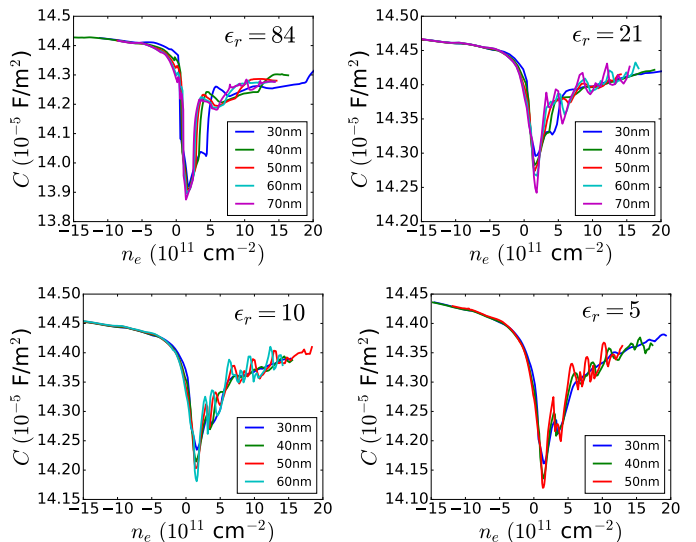


FIG. 4: Total capacitances of 30-70nm quantum wells with dielectric constants $\epsilon_r = 84, 21, 10, 5$. $C_{\text{in}} = 1.45 \times 10^{-22} \text{F/nm}^2$ is used as estimated in experiment¹³.

adjust the carrier density in the quantum well and then convert it to the corresponding gate voltage $V_g(\mu)$ by:

$$\begin{aligned} eV_g &= eV_{\text{in}} + \mu - \mu_0 \\ &= \frac{e^2 n_e}{C_{\text{in}}} + \mu - \mu_0 \end{aligned} \quad (7)$$

where V_{in} the electric voltage drop across the insulator between top gate and HgTe, C_{in} is the geometric capacitance of the insulator and μ_0 is the chemical potential in flat band condition. Take the derivative with respect to n_e on both sides of Eq.(7):

$$\frac{1}{e} \frac{dV_g}{dn_e} = \frac{1}{C_{\text{in}}} + \frac{1}{e^2} \frac{d\mu}{dn_e} \quad (8)$$

then the total capacitance C can be expressed as:

$$\frac{1}{C} = \frac{1}{C_{\text{in}}} + \frac{1}{e^2} \frac{dn_e}{d\mu} \quad (9)$$

Total capacitances for 30-70nm HgTe quantum wells are shown in FIG.4, which is consistent with recent experimental result¹³. Compare with the experiment, $e^2 dn_e/d\mu$ term in Eq.(9) consists of the quantum capacitances from top ($e^2 D_t$) and bottom ($e^2 D_b$) interfaces and the geometric capacitance of the HgTe well (C_{tb}):

$$e^2 \frac{dn_e}{d\mu} = e^2 D_t + \left(\frac{1}{C_{\text{tb}}} + \frac{1}{e^2 D_b} \right)^{-1} \quad (10)$$

where D_t and D_b are thermodynamic density of states of top and bottom interfaces respectively.

The quantum effect, as a result of the Pauli exclusion principle, is negligible for metals with infinitely large

thermodynamic DoS. When the DoS getting smaller and ultimately comparable with the geometric capacitance, the quantum effect starts playing an important role: decreasing (increasing) the total capacitance if the thermodynamic DoS, $dn_e/d\mu$, is positive (negative). Negative thermodynamic DoS is also known as negative compressibility. As shown in FIG.4, the total capacitance reveals a depression when the chemical potential is tuned within the bulk gap, where the DoS is pretty small. The capacitance deep in the hole-dominant region is larger than the electron-dominant region. This can be simply explained by the band structure: the DoS of the valence bands is larger than that of conduction bands.

Compare the capacitances with different dielectric constants in FIG.4, the overall shape of the line is getting smoother when the dielectric constant is getting smaller. That indicates the Fermi level is resisted to be tuned into the quasi-2D conduction and valence bands. It is consis-

tent with what we expected in section III.

V. THERMOELECTRIC TRANSPORT

Our theoretical band structure model can also provide convincing thermoelectric transport results within the semiclassical regime, $\omega_c\tau \ll 1$, here $\omega_c = \frac{eB}{m}$ is the cyclotron frequency.

Consider the linear response to weak fields, the electric current density is expressed as:

$$\mathbf{J} = \sigma \mathbf{\Sigma} + \alpha(-\nabla T) \quad (11)$$

where $\mathbf{\Sigma} = \mathbf{E} + \frac{1}{e}\nabla\mu$ and μ is the chemical potential. Generally, σ and α are tensors. Under the relaxation time approximation and consider a uniform and spatially uniform magnetic field \mathbf{B} , the electric current density is:

$$\mathbf{J} = -e \int \frac{d^2\mathbf{k}}{(2\pi)^2} \left(-\frac{\partial f^0(\varepsilon_{\mathbf{k}})}{\partial \varepsilon_{\mathbf{k}}} \right) \mathbf{v}(\mathbf{k}) \left[\tau \mathbf{v}(\mathbf{k}) + \tau^2 \frac{e}{\hbar c} (\mathbf{v}(\mathbf{k}) \times \mathbf{B})_{\alpha} \frac{\partial \mathbf{v}(\mathbf{k})}{\partial k_{\alpha}} \right] \cdot \left[-e\mathbf{\Sigma} + \frac{\varepsilon(\mathbf{k}) - \mu}{T} (-\nabla T) \right] \quad (12)$$

where a constant scattering time τ is assumed. Details of derivation of Eq.(12) are in Appendix B. Compare Eqs.(11) and (12), we get expressions of conductivity σ and coefficient α in terms of 2D k -space integration, showed in Appendix B. For low external field, $\omega_c\tau \ll 1$, Onsager relation $\sigma_{\mu\nu}(B) = \sigma_{\nu\mu}(-B)$ restricts the leading order term of longitudinal and transverse coefficients to be:

$$\begin{aligned} \sigma_{xx}, \alpha_{xx} &\sim \tau \\ \sigma_{xy}, \alpha_{xy} &\sim \omega_c\tau^2 \end{aligned} \quad (13)$$

Consider the case that the temperature gradient is applied in x direction, then the thermopower S_{xx} and the Nernst coefficient S_{xy} are:

$$\begin{aligned} S_{xx} &= \frac{E_x}{\nabla_x T} = \frac{\alpha_{xx}\sigma_{yy} - \alpha_{yx}\sigma_{xy}}{\sigma_{xx}\sigma_{yy} - \sigma_{yx}\sigma_{xy}} \\ S_{xy} &= \frac{E_y}{\nabla_x T} = \frac{\alpha_{xx}\sigma_{yx} - \alpha_{yx}\sigma_{xx}}{\sigma_{xy}\sigma_{yx} - \sigma_{yy}\sigma_{xx}} \end{aligned} \quad (14)$$

Inspired by Eq.(13), we could safely ignore the terms $\sigma_{xy}\alpha_{yx} \propto (\omega_c\tau)^2$ and $\sigma_{xy}\sigma_{yx} \propto (\omega_c\tau)^2$ in Eq.(14). Then,

$$\begin{aligned} S_{xx} &\approx \frac{\alpha_{xx}}{\sigma_{xx}} \\ S_{xy} &\approx \frac{\alpha_{yx}\sigma_{xx} - \alpha_{xx}\sigma_{yx}}{\sigma_{yy}\sigma_{xx}} \end{aligned} \quad (15)$$

By simplified the problem with a constant scattering time and weak external field, the thermopower only depends on the band structure and the Nernst coefficient is proportional to $B\tau$ times a quantity which also only depends on the band structure.

Seebeck coefficients for 30-70nm HgTe quantum wells at a low temperature without the magnetic field are shown in FIG.5. And the Nernst effect for a 60nm quantum well is shown in FIG.6. They agree well with recent thermoelectric transport experiments¹⁴, where the Seebeck and Nernst coefficients are quite large on the hole-dominant side compared with the electron-dominant side. In our calculated results, the Seebeck and Nernst coefficients both change sign on hole- and electron-dominant sides. In the transport experiment¹⁴, the Seebeck coefficient changes sign while the Nernst coefficient keeps the same sign. That indicates that when the band structure getting complicated deep into the valence bands, the constant scattering time approximation used in our model is not a proper model to capture all effects.

VI. CONCLUSIONS

According to the capacitance results both from experiments and our numerical results, the Fermi level can be easily tuned into the quasi-2D conduction and valence bands. When the Fermi level is inside the bulk gap, the maximum carrier density is around $4 \times 10^{11} \text{cm}^{-2}$ for 30-70nm quantum wells. The dielectric constant is estimated to be $\epsilon_r \approx 6$, and the small dielectric constant tries to maintain the Fermi level inside the bulk gap due to the 2D linear dispersion and the large localization length of the surface states.

The phenomenological effective potential¹² for the sake of keeping the Fermi level within the bulk gap is not proper. Quantum Hall plateaus observed in magneto-

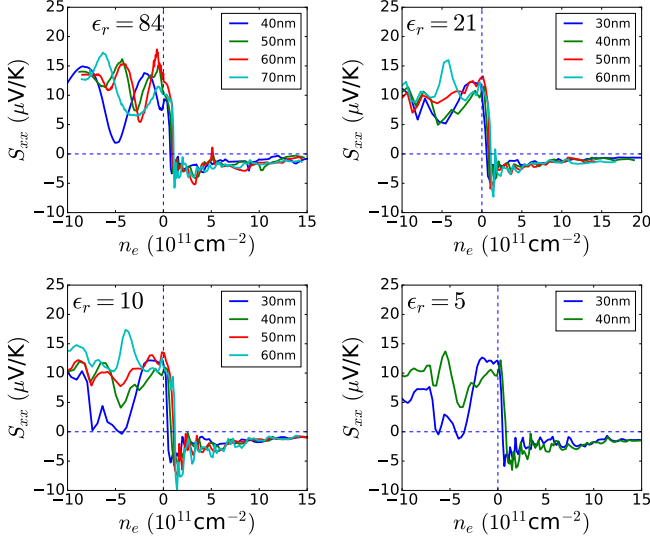


FIG. 5: Seebeck coefficients at $B = 0$ for 30-70nm HgTe quantum wells. Holes dominate on the left side of the vertical dashed line while electrons dominate on the right side. The thermopower of the hole-dominant carriers are much larger than that of electron-dominant carriers.

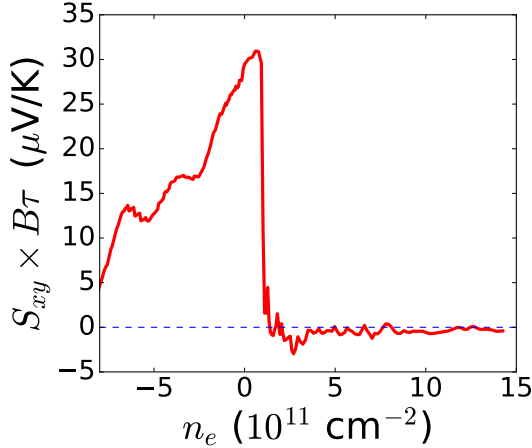


FIG. 6: Nernst coefficient at weak magnetic field for the 60nm quantum well. $\epsilon_r = 84$. On the hole side, the Nernst coefficient is larger than the electron side. It changes sign from hole- to electron-side.

transport studies^{9,12} imply that the transport is surface-state dominated, whereas this is not the evidence that only the surface states are occupied. Inconspicuous quantized Hall resistance and non-zero longitudinal resistivity measurements ρ_{xx} give a clue that quasi-2D conduction bands are also occupied, especially for high gate voltages.

Our model shows that the thermopower is fairly large on the hole-dominated side compared to that on the electron-dominated side. The agreement with thermopower experimental results indicates that the asymmetric of the thermopower is a direct result of the band structure. The proposed¹⁴ phonon drag effect to explain the thermopower asymmetry is not necessary. By using the semiclassical transport model simplified by constant scattering time approximation, our model can capture the shape of the Nernst coefficient versus carrier density, that is, the Nernst coefficient is larger on the hole-dominated side than electron-dominated side. The sign, however, of the Nernst coefficient does not match the experiment. This indicates the constant scattering time approximation is not enough to capture all effects in this system.

Appendix A: Model Hamiltonian of Strained HgTe

Choose the 8-band basis set¹⁵:

$$\begin{aligned}
 u_1(\mathbf{r}) &= |\Gamma_6, +\frac{1}{2}\rangle = S \uparrow \\
 u_2(\mathbf{r}) &= |\Gamma_6, -\frac{1}{2}\rangle = S \downarrow \\
 u_3(\mathbf{r}) &= |\Gamma_8, +\frac{3}{2}\rangle = \frac{1}{\sqrt{2}}(X + iY) \uparrow \\
 u_4(\mathbf{r}) &= |\Gamma_8, +\frac{1}{2}\rangle = \frac{1}{\sqrt{6}}[(X + iY) \downarrow - 2Z \uparrow] \\
 u_5(\mathbf{r}) &= |\Gamma_8, -\frac{1}{2}\rangle = -\frac{1}{\sqrt{6}}[(X - iY) \uparrow + 2Z \downarrow] \\
 u_6(\mathbf{r}) &= |\Gamma_8, -\frac{3}{2}\rangle = -\frac{1}{\sqrt{2}}(X - iY) \downarrow \\
 u_7(\mathbf{r}) &= |\Gamma_7, +\frac{1}{2}\rangle = \frac{1}{\sqrt{3}}[(X + iY) \downarrow + Z \uparrow] \\
 u_8(\mathbf{r}) &= |\Gamma_7, -\frac{1}{2}\rangle = \frac{1}{\sqrt{3}}[(X - iY) \uparrow - Z \downarrow]
 \end{aligned} \tag{A1}$$

The corresponding Hamiltonian of the quantum well with [001] growth direction is

$$H = \begin{pmatrix} T & 0 & -\frac{1}{\sqrt{2}}Pk_+ & \sqrt{\frac{2}{3}}Pk_z & \frac{1}{\sqrt{6}}Pk_- & 0 & -\frac{1}{\sqrt{3}}Pk_z & -\frac{1}{\sqrt{3}}Pk_- \\ 0 & T & 0 & -\frac{1}{\sqrt{6}}Pk_+ & \sqrt{\frac{2}{3}}Pk_z & \frac{1}{\sqrt{2}}Pk_- & -\frac{1}{\sqrt{3}}Pk_+ & \frac{1}{\sqrt{3}}Pk_z \\ -\frac{1}{\sqrt{2}}k_-P & 0 & U+V & -\bar{S}_- & R & 0 & \frac{1}{\sqrt{2}}\bar{S}_- & -\sqrt{2}R \\ \sqrt{\frac{2}{3}}k_zP & -\frac{1}{\sqrt{6}}k_-P & -\bar{S}_-^\dagger & U-V & C & R & \sqrt{2}V & -\sqrt{\frac{3}{2}}\tilde{S}_- \\ \frac{1}{\sqrt{6}}k_+P & \sqrt{\frac{2}{3}}k_zP & R^\dagger & C^\dagger & U-V & \bar{S}_+^\dagger & -\sqrt{\frac{3}{2}}\tilde{S}_+ & -\sqrt{2}V \\ 0 & \frac{1}{\sqrt{2}}k_+P & 0 & R^\dagger & \bar{S}_+ & U+V & \sqrt{2}R^\dagger & \frac{1}{\sqrt{2}}\bar{S}_+ \\ -\frac{1}{\sqrt{3}}k_zP & -\frac{1}{\sqrt{3}}k_-P & \frac{1}{\sqrt{2}}\bar{S}_-^\dagger & \sqrt{2}V & -\sqrt{\frac{3}{2}}\tilde{S}_+^\dagger & \sqrt{2}R & U-\Delta & C \\ -\frac{1}{\sqrt{3}}k_+P & \frac{1}{\sqrt{3}}k_zP & -\sqrt{2}R^\dagger & -\sqrt{\frac{3}{2}}\tilde{S}_-^\dagger & -\sqrt{2}V & \frac{1}{\sqrt{2}}\bar{S}_+^\dagger & C^\dagger & U-\Delta \end{pmatrix} \quad (\text{A2})$$

where the elements in the matrix are

$$\begin{aligned} k_{\parallel}^2 &= k_x^2 + k_y^2, \quad k_{\pm} = k_x \pm ik_y, \quad k_z = -i\partial_z \\ T &= E_c(z) + \frac{\hbar^2}{2m_0}[(2F+1)k_{\parallel}^2 + k_z(2F+1)k_z] \\ U &= E_v(z) - \frac{\hbar^2}{2m_0}(\gamma_1 k_{\parallel}^2 + k_z\gamma_1 k_z) \\ V &= -\frac{\hbar^2}{2m_0}(\gamma_2 k_{\parallel}^2 - 2k_z\gamma_2 k_z) \\ R &= -\sqrt{3}\frac{\hbar^2}{2m_0}(\mu k_+^2 - \bar{\gamma} k_-^2) = \sqrt{3}\frac{\hbar^2}{2m_0}[\gamma_2(k_x^2 - k_y^2) - 2i\gamma_3 k_x k_y] \\ \bar{S}_{\pm} &= -\sqrt{3}\frac{\hbar^2}{2m_0}k_{\pm}(\{\gamma_3, k_z\} + [\kappa, k_z]) \\ \tilde{S}_{\pm} &= -\sqrt{3}\frac{\hbar^2}{2m_0}k_{\pm}(\{\gamma_3, k_z\} - \frac{1}{3}[\kappa, k_z]) \\ C &= 2\frac{\hbar^2}{2m_0}k_-[\kappa, k_z] \end{aligned} \quad (\text{A3})$$

The effects of strain are added to the Hamiltonian through the Bir-Pikus Hamiltonian^{9,11}:

$$H_{nn'} \rightarrow H_{nn'} + H_{nn'}^{BP} \quad (\text{A4})$$

H^{BP} is derived from the Hamiltonian without strain by substitution:

$$k_i k_j \rightarrow \varepsilon_{ij} \quad (\text{A5})$$

and the band structure parameters are replaced by:

$$\begin{aligned} \frac{\hbar^2}{2m_0}(2F+1) &\rightarrow a_c \\ \frac{\hbar^2}{m_0}\gamma_1 &\rightarrow -2a_v \\ \frac{\hbar^2}{m_0}\gamma_2 &\rightarrow -b \\ \frac{\hbar^2}{m_0}\gamma_3 &\rightarrow -d/\sqrt{3} \end{aligned} \quad (\text{A6})$$

where⁹

$$\begin{aligned} a_c &= -4.6\text{eV}, \\ a_v &= -0.13\text{eV}, \\ b &= -1.15\text{eV}, \\ C_{12}/C_{11} &= 0.68 \end{aligned} \quad (\text{A7})$$

a_c and a_v are the hydrostatic deformation potentials of the conduction and valence bands, respectively, and b, d are uniaxial deformation potentials.

Appendix B: Thermoelectric Effects Under Weak Fields

Seebeck effect is the longitudinal thermoelectric voltage induced by a temperature gradient, and Nernst effect is the transverse thermoelectric response of a temperature gradient under a out-of-plane magnetic field. Microscopic theory of these thermoelectric effects in the semi-classical picture can be described with the Boltzmann

equation in steady state:

$$\mathbf{v}(\mathbf{k}) \cdot \nabla_{\mathbf{r}} f_{\mathbf{k}}^0 + \frac{\mathbf{F}}{\hbar} \cdot \nabla_{\mathbf{k}} f_{\mathbf{k}}^0 = \left(\frac{\partial f}{\partial t} \right)_{\text{coll}} \quad (\text{B1})$$

where $f_{\mathbf{k}}^0 = (e^{(\varepsilon_{\mathbf{k}} - \mu)/k_{\text{B}}T} + 1)^{-1}$ is the Fermi-Dirac distribution function describing the equilibrium state, $f = f(\mathbf{r}, \mathbf{k}, t)$ is the distribution function deviating from the equilibrium, \mathbf{F} is the external forces induced by electric field, magnetic field or temperature gradient. The right hand side of Eq.(B1) is the collision effect. Here we consider the relaxation time approximation for simplicity:

$$\left(\frac{\partial f}{\partial t} \right)_{\text{coll}} = -\frac{1}{\tau} (f(\mathbf{r}, \mathbf{k}, t) - f_{\mathbf{k}}^0) \quad (\text{B2})$$

where a constant relaxation time τ is assumed.

The solution of Eq.(B1) is²¹:

$$f_{\mathbf{k}}(t) - f_{\mathbf{k}}^0 = - \int_{-\infty}^t dt' P(t, t') \frac{df_{\mathbf{k}}^0}{dt'} \quad (\text{B3})$$

where $P(t, t') = e^{-(t-t')/\tau}$ is the fraction of electrons survive from t' to t without collisions. With semiclassical equations of motion:

$$\begin{aligned} \dot{\mathbf{r}} &= \mathbf{v}(\mathbf{k}) = \frac{1}{\hbar} \frac{\partial \varepsilon_{\mathbf{k}}}{\partial \mathbf{k}} \\ \hbar \dot{\mathbf{k}} &= -e [\mathbf{E}(\mathbf{r}, t) + \frac{1}{c} \mathbf{v}(\mathbf{k}) \times \mathbf{B}(\mathbf{r}, t)] \end{aligned} \quad (\text{B4})$$

and use the fact that:

$$\begin{aligned} \frac{df_{\mathbf{k}}^0}{dt} &= \frac{d\mathbf{k}}{dt} \cdot \nabla_{\mathbf{k}} f_{\mathbf{k}}^0 + \frac{d\mathbf{r}}{dt} \cdot \nabla_{\mathbf{r}} f_{\mathbf{k}}^0 \\ \frac{1}{\hbar} \nabla_{\mathbf{k}} f_{\mathbf{k}}^0 &= \mathbf{v}(\mathbf{k}) \frac{\partial f_{\mathbf{k}}^0}{\partial \varepsilon_{\mathbf{k}}} \\ \nabla_{\mathbf{r}} f_{\mathbf{k}}^0 &= \frac{\partial f_{\mathbf{k}}^0}{\partial T} \nabla_{\mathbf{r}} T + \frac{\partial f_{\mathbf{k}}^0}{\partial \mu} \nabla_{\mathbf{r}} \mu \end{aligned} \quad (\text{B5})$$

then

$$\begin{aligned} f_{\mathbf{k}}(t) - f_{\mathbf{k}}^0 &= \int_{-\infty}^t dt' e^{-(t-t')/\tau} \left(- \frac{\partial f_{\mathbf{k}}^0}{\partial \varepsilon_{\mathbf{k}}} \right) \mathbf{v}(\mathbf{k}(t')) \cdot \\ &\quad \left[-e\mathbf{E}(t') - \nabla_{\mathbf{r}} \mu(t') - \frac{\varepsilon_{\mathbf{k}} - \mu}{T} \nabla_{\mathbf{r}} T \right] \end{aligned} \quad (\text{B6})$$

The magnetic field is out of the Eq.(B6) if it is perpendicular to the transport plane, $\mathbf{B} = B\hat{z}$.

The deviation function $\phi_{\mathbf{k}}$, defined by $f_{\mathbf{k}} \approx f_{\mathbf{k}}^0 - \frac{\partial f_{\mathbf{k}}^0}{\partial \varepsilon_{\mathbf{k}}} \phi_{\mathbf{k}}$, is directly derived from Eq.(B6):

$$\begin{aligned} \phi_{\mathbf{k}}(t) &= \int_0^{\infty} dt'' e^{-t''/\tau} \mathbf{v}(\mathbf{k} - t''\dot{\mathbf{k}}) \cdot \left[-e\mathbf{E}(t - t'') \right. \\ &\quad \left. - \nabla_{\mathbf{r}} \mu(t - t'') - \frac{\varepsilon_{\mathbf{k}} - \mu}{T} \nabla_{\mathbf{r}} T(t - t'') \right] \end{aligned} \quad (\text{B7})$$

where $t'' = t - t'$. Ignore the time dependence of \mathbf{E} , μ and T , and use

$$\begin{aligned} \mathbf{k}(t - t'') &= \mathbf{k}(t) - t''\dot{\mathbf{k}} \\ \mathbf{v}(\mathbf{k} - t''\dot{\mathbf{k}}) &= \mathbf{v}(\mathbf{k}) - t''\dot{\mathbf{k}} \cdot \frac{\partial \mathbf{v}}{\partial \mathbf{k}} \end{aligned} \quad (\text{B8})$$

then to the first order in fields,

$$\begin{aligned} \phi_{\mathbf{k}} &= \left[\tau \mathbf{v}(\mathbf{k}) + \tau^2 \frac{eB}{\hbar c} (\mathbf{v}(\mathbf{k}) \times \hat{z})_{\alpha} \frac{\partial \mathbf{v}(\mathbf{k})}{\partial k_{\alpha}} \right] \cdot \\ &\quad \left[-e\boldsymbol{\Sigma} + \frac{\varepsilon_{\mathbf{k}} - \mu}{T} (-\nabla T) \right] \end{aligned} \quad (\text{B9})$$

where $\boldsymbol{\Sigma} = \mathbf{E} + \frac{1}{c} \nabla \mu$. Here we ignore the spatial subscript in the gradient label ∇ , and subscript α is the Einstein notation.

The electric current density is expressed as

$$\begin{aligned} \mathbf{J} &= -e \int \frac{d^2 \mathbf{k}}{(2\pi)^2} \mathbf{v}(\mathbf{k}) \left(- \frac{\partial f_{\mathbf{k}}^0}{\partial \varepsilon_{\mathbf{k}}} \right) \phi_{\mathbf{k}} \\ &= -e \int \frac{d^2 \mathbf{k}}{(2\pi)^2} \mathbf{v}(\mathbf{k}) \left(- \frac{\partial f_{\mathbf{k}}^0}{\partial \varepsilon_{\mathbf{k}}} \right) \left[\tau \mathbf{v}(\mathbf{k}) + \right. \\ &\quad \left. \tau^2 \frac{eB}{\hbar c} (\mathbf{v}(\mathbf{k}) \times \hat{z})_{\alpha} \frac{\partial \mathbf{v}(\mathbf{k})}{\partial k_{\alpha}} \right] \cdot \left[-e\boldsymbol{\Sigma} + \right. \\ &\quad \left. \frac{\varepsilon_{\mathbf{k}} - \mu}{T} (-\nabla T) \right] \\ &= \sigma \boldsymbol{\Sigma} + \alpha (-\nabla T) \end{aligned} \quad (\text{B10})$$

where

$$\begin{aligned} \sigma &= e^2 \int \frac{d^2 \mathbf{k}}{(2\pi)^2} \left(- \frac{\partial f_{\mathbf{k}}^0}{\partial \varepsilon_{\mathbf{k}}} \right) \mathbf{v}(\mathbf{k}) \cdot \\ &\quad \left[\tau \mathbf{v}(\mathbf{k}) + \tau^2 \frac{eB}{\hbar c} (\mathbf{v}(\mathbf{k}) \times \hat{z})_{\alpha} \frac{\partial \mathbf{v}(\mathbf{k})}{\partial k_{\alpha}} \right] \end{aligned} \quad (\text{B11})$$

$$\begin{aligned} \alpha &= \frac{-e}{T} \int \frac{d^2 \mathbf{k}}{(2\pi)^2} \left(- \frac{\partial f_{\mathbf{k}}^0}{\partial \varepsilon_{\mathbf{k}}} \right) (\varepsilon_{\mathbf{k}} - \mu) \mathbf{v}(\mathbf{k}) \cdot \\ &\quad \left[\tau \mathbf{v}(\mathbf{k}) + \tau^2 \frac{eB}{\hbar c} (\mathbf{v}(\mathbf{k}) \times \hat{z})_{\alpha} \frac{\partial \mathbf{v}(\mathbf{k})}{\partial k_{\alpha}} \right] \end{aligned} \quad (\text{B12})$$

σ and α both satisfy the Onsager relation $\sigma_{\mu\nu}(B) = \sigma_{\nu\mu}(-B)$. To the leading order in magnetic field, the Onsager relation leads to:

$$\begin{aligned} \sigma_{xx}, \sigma_{yy}, \alpha_{xx}, \alpha_{yy} &\sim \tau \\ \sigma_{xy}, \sigma_{yx}, \alpha_{xy}, \alpha_{yx} &\sim \omega_c \tau^2 \end{aligned} \quad (\text{B13})$$

where $\omega_c = \frac{eB}{m}$ is the cyclotron frequency. Specifically,

$$\begin{aligned} \sigma_{xx} &= e^2 \tau \int \frac{d^2 \mathbf{k}}{(2\pi)^2} \left(- \frac{\partial f_{\mathbf{k}}^0}{\partial \varepsilon_{\mathbf{k}}} \right) v_x^2 \\ \alpha_{xx} &= \frac{-e\tau}{T} \int \frac{d^2 \mathbf{k}}{(2\pi)^2} \left(- \frac{\partial f_{\mathbf{k}}^0}{\partial \varepsilon_{\mathbf{k}}} \right) (\varepsilon_{\mathbf{k}} - \mu) v_x^2 \\ \sigma_{xy} &= \tau^2 \frac{e^3 B}{\hbar c} \int \frac{d^2 \mathbf{k}}{(2\pi)^2} \\ &\quad \left(- \frac{\partial f_{\mathbf{k}}^0}{\partial \varepsilon_{\mathbf{k}}} \right) v_x \left(v_y \frac{\partial v_y}{\partial k_x} - v_x \frac{\partial v_y}{\partial k_y} \right) \\ \alpha_{xy} &= -\frac{\tau^2 e^2 B}{T \hbar c} \int \frac{d^2 \mathbf{k}}{(2\pi)^2} \\ &\quad \left(- \frac{\partial f_{\mathbf{k}}^0}{\partial \varepsilon_{\mathbf{k}}} \right) (\varepsilon_{\mathbf{k}} - \mu) v_x \left(v_y \frac{\partial v_y}{\partial k_x} - v_x \frac{\partial v_y}{\partial k_y} \right) \end{aligned} \quad (\text{B14})$$

Consider the case that the temperature gradient is applied in x direction. The thermopower S_{xx} and Nernst effect coefficient S_{xy} are defined as

$$\begin{aligned} S_{xx} &= \frac{E_x}{\nabla_x T} = \frac{\alpha_{xx}\sigma_{yy} - \alpha_{yx}\sigma_{xy}}{\sigma_{xx}\sigma_{yy} - \sigma_{yx}\sigma_{xy}} \\ S_{xy} &= \frac{E_y}{\nabla_x T} = \frac{\alpha_{xx}\sigma_{yx} - \alpha_{yx}\sigma_{xx}}{\sigma_{xy}\sigma_{yx} - \sigma_{yy}\sigma_{xx}} \end{aligned} \quad (\text{B15})$$

We can safely ignore the magnetic field's high-order terms in Eq.(B15), then

$$\begin{aligned} S_{xx} &\approx \frac{\alpha_{xx}}{\sigma_{xx}} \\ S_{xy} &\approx \frac{\alpha_{yx}\sigma_{xx} - \alpha_{xx}\sigma_{yx}}{\sigma_{yy}\sigma_{xx}} \end{aligned} \quad (\text{B16})$$

and σ, α are expressed in Eq.(B14).

ACKNOWLEDGMENTS

The authors would like to thank B. Xiong, C. Xiao, M. Xie, F. Xue and T. Lovorn for helpful discussions. This work was supported by the Army Research Office (ARO) under contract W911NF-15-1-0561:P00001, and by the Welch Foundation under grant TBF1473. The authors acknowledge the Texas Advanced Computing Center (TACC) at The University of Texas at Austin for providing HPC, visualization, database and grid resources that have contributed to the research results reported within this paper.

-
- ¹ M. Z. Hasan and C. L. Kane, *Rev. Mod. Phys.* **82**, 3045 (2010).
 - ² X.-L. Qi and S.-C. Zhang, *Rev. Mod. Phys.* **83**, 1057 (2011).
 - ³ L. Fu and C. L. Kane, *Phys. Rev. B* **76**, 045302 (2007).
 - ⁴ J. Wiedenmann, E. Bocquillon, R. S. Deacon, S. Hartinger, O. Herrmann, T. M. Klapwijk, L. Maier, C. Ames, C. Brne, and C. Gould, *Nature communications* **7**, 10303 (2016).
 - ⁵ S. Hart, H. Ren, M. Kosowsky, G. Ben-Shach, P. Leubner, C. Brne, H. Buhmann, L. W. Molenkamp, B. I. Halperin, and A. Yacoby, *Nature Physics* **13**, 87 (2016).
 - ⁶ E. Bocquillon, R. S. Deacon, J. Wiedenmann, P. Leubner, T. M. Klapwijk, C. Brne, K. Ishibashi, H. Buhmann, and L. W. Molenkamp, *Nature Nanotechnology* **12**, 137 (2016).
 - ⁷ S. Hart, H. Ren, T. Wagner, P. Leubner, M. Mhlbauer, C. Brne, H. Buhmann, L. W. Molenkamp, and A. Yacoby, *Nature Physics* **10**, 638 (2014).
 - ⁸ I. Sochnikov, L. Maier, C. A. Watson, J. R. Kirtley, C. Gould, G. Tkachov, E. M. Hankiewicz, C. Brüne, H. Buhmann, L. W. Molenkamp, and K. A. Moler, *Phys. Rev. Lett.* **114**, 066801 (2015).
 - ⁹ C. Brüne, C. X. Liu, E. G. Novik, E. M. Hankiewicz, H. Buhmann, Y. L. Chen, X. L. Qi, Z. X. Shen, S. C. Zhang, and L. W. Molenkamp, *Phys. Rev. Lett.* **106**, 126803 (2011).
 - ¹⁰ A. Budewitz, K. Bendias, P. Leubner, T. Khouri, S. Shamim, S. Wiedmann, H. Buhmann, and L. Molenkamp, *arXiv preprint arXiv:1706.05789* (2017).
 - ¹¹ M. Korkusinski and P. Hawrylak, *Sci. Rep.* **4** (2014).
 - ¹² C. Brüne, C. Thienel, M. Stuiber, J. Böttcher, H. Buhmann, E. G. Novik, C.-X. Liu, E. M. Hankiewicz, and L. W. Molenkamp, *Phys. Rev. X* **4**, 041045 (2014).
 - ¹³ D. A. Kozlov, D. Bauer, J. Ziegler, R. Fischer, M. L. Savchenko, Z. D. Kvon, N. N. Mikhailov, S. A. Dvoretzky, and D. Weiss, *Phys. Rev. Lett.* **116**, 166802 (2016).
 - ¹⁴ A. Jost, M. Bendias, J. Böttcher, E. Hankiewicz, C. Brüne, H. Buhmann, L. W. Molenkamp, J. C. Maan, U. Zeitler, N. Hussey, *et al.*, *Proc. Natl. Acad. Sci. U.S.A.* **114**, 3381 (2017).
 - ¹⁵ E. G. Novik, A. Pfeuffer-Jeschke, T. Jungwirth, V. Latussek, C. R. Becker, G. Landwehr, H. Buhmann, and L. W. Molenkamp, *Phys. Rev. B* **72**, 035321 (2005).
 - ¹⁶ A. H. MacDonald, S. H. Vosko, and P. T. Coleridge, *Journal of Physics C: Solid State Physics* **12**, 2991 (1979).
 - ¹⁷ *Texas Advanced Computing Center (TACC), The University of Texas at Austin.*
 - ¹⁸ J. Baars and F. Sorger, *Solid St. Commun.* **10**, 875 (1972).
 - ¹⁹ M. Grynberg, R. Le Toullec, and M. Balkanski, *Phys. Rev. B* **9**, 517 (1974).
 - ²⁰ A. M. Shuvaev, G. V. Astakhov, G. Tkachov, C. Brüne, H. Buhmann, L. W. Molenkamp, and A. Pimenov, *Phys. Rev. B* **87**, 121104 (2013).
 - ²¹ N. W. Ashcroft and N. D. Mermin, *Solid state physics* (Holt, Rinehart and Winston, 1976).